Detailed Characteristics of Drop-Laden Mixing Layers: LES Predictions compared to DNS

Nora Okong'o*, Anthony Leboissetier† and Josette Bellan‡
Jet Propulsion Laboratory
California Institute of Technology
Pasadena CA 91109-8099

Results have been compared from Direct Numerical Simulation (DNS) and Large Eddy Simulation (LES) of a temporal mixing layer laden with evaporating drops, to assess the ability of LES to reproduce detailed characteristics of DNS. The LES used computational drops, each of which represented eight physical drops, and a reduced flow field resolution using a grid spacing four times larger than that of the DNS. The LES used models for the filtered source terms (FST), which express the coupling of the drops with the flow, and for the unresolved Subgrid Scale (SGS) fluxes of species-mass, momentum and enthalpy. The LES were conducted using one of three different SGS-flux models: dynamic-coefficient Gradient (GRD), dynamic-coefficient Smagorinsky (SMD) and constant-coefficient Scale-Similarity (SSC). The comparison of the filtered coarsened (FC) DNS to the LES considered detailed aspects of the flow that are of interest in ignition or full combustion. All LES captured the largest-scale vortex, the global amount of vapor emanating from the drops and the overall size distribution of the drops. All LES tended to underpredict the global amount of irreversible entropy production (dissipation). The SMD model was found unable to capture either the global or local voriticity variation, and had minimal small-scale activity in dynamic and thermodynamic variables compared to the FC-DNS. The SMD model was also deficient in predicting the spatial distribution of drops and of the dissipation. In contrast, the GRD and SSC models did mimic the small-scale activity of the FC-DNS, and the spatial distribution of drops and of the dissipation. Therefore, the GRD and SSC models are recommended, while the SMD model seems inappropriate, for combustion or other problems where the local activity must be predicted.

1 Introduction

Direct Numerical Simulation (DNS) is a methodology wherein all scales of the flow are resolved. For two-phase (TP) flows with particles that are much smaller than the Kolmogorov scale and which have a volumetrically small loading ($\simeq 10^{-3}$), Boivin et al.[1] have shown that the drops can be treated as point sources of mass, momentum and energy from the gas-phase perspective. In such situations, it is appropriate to perform simulations using a gas-phase resolution that is adequate for single-phase (SP) flow, using an Eulerian framework to describe the gas phase and a Lagrangian framework to track the drops. The terminology DNS, while not strictly accurate, is traditionally applied to such simulations. Several recent studies have used this DNS methodology,[1-5] and we have used it for DNS of a transitional temporal mixing layer with evaporating drops.[6-8]

Large Eddy Simulation (LES), in which only the large scales need to be resolved, is a promising alternative to DNS. LES may be conducted with reduced flow field resolution compared to DNS and using 'computational' drops to represent the physical drops. The LES gas-phase equations are derived by filtering the DNS gas-phase equations, leading to unclosed terms: the subgrid-scale (SGS) fluxes that arise from the convective terms and the filtered source terms (FSTs) that embody the effect of the drops on the resolved flow field. Recent LES of TP flows have considered an incompressible gas phase laden with small solid particles, with one-way[9-14] or two-way[9,14] coupling, and used physical or computational particles whose evolution was entirely governed by the resolved flow field, that is, neglecting SGS effects on drop evolution. For the situation of liquid drops, the liquid is $O\left(10^3\right)$ times denser than the carrier gas, so the mass loadings can be significant ($\gtrsim 10^{-1}$) despite a low volumetric loading; therefore, the drops may considerably influence the flow and this two-way coupling must be modeled. Furthermore, a compressible formulation is required due to the density changes induced by the drop vapor, and the thermodynamic variables are coupled through the equation of state, as well as through the heat and mass fluxes appearing in the energy and species equations. Therefore, appropriate modeling of the momentum, energy and species SGS fluxes must be carefully assessed, with due consideration to the form of the energy equation.[15-17] Using our DNS of

*Scientist, AIAA Senior Member.

†Post-Doctoral Scholar, AIAA Member.

‡Senior Research Scientist, AIAA Associate Fellow (corresponding author, josette.bellan@jpl.nasa.gov).

a temporal mixing layer[8] and extending previous SGS TP flow models,[7,18] we have developed LES models and have tested them, both *a priori* (using a DNS database[8]) and *a posteriori* (by performing LES[19]) .

In this paper, we analyze the detailed characteristics of the layer, in order to assess whether the LES can predict aspects of the flow that are of interest in combustion applications. This paper is organized as follows: In Section 2 we present the highlights of the DNS formulation, followed by a summary of the LES method in Section 3. Section 4 contains the analysis of the detailed characteristics predicted by LES, with conclusions in Section 5.

2 DNS Methodology

Details of the DNS method have been given by Okong'o and Bellan,[8] based on the formulation of Miller and Bellan.[6] Here we summarize the gas-phase and liquid-phase equations, the flow configuration and the numerical procedure.

2.1 Gas-phase equations

We define the vector of gas-phase conservative variables $\phi = \{\rho,\ \rho u_i,\ \rho e_t,\ \rho Y_V\}$ and denote the flow field as ϕ, where ρ is the density, u_i is the velocity in the x_i coordinate direction, e_t is the total energy and Y_V is the vapor (subscript V) mass fraction (the carrier gas, subscript C, mass fraction is Y_C; $Y_C + Y_V = 1$). The DNS gas-phase conservation equations are:

$$\frac{\partial \phi}{\partial t} + \frac{\partial \left(\phi u_j\right)}{\partial x_j} = \frac{\partial \left[\Theta_j(\phi)\right]}{\partial x_j} + S, \tag{1}$$

where $S = \{S_I, S_{II,i}, S_{III}, S_I\}$ are source terms due to the action of the drops and

$$\Theta_j\left(\phi\right) = \{0, \sigma_{ij} - p\delta_{ij}, \sigma_{ij}u_i - q_j - pu_j, -j_{Vj}\}. \tag{2}$$

The thermodynamic variables to be computed from ϕ are the internal energy ($e = e_t - u_i u_i/2$), the pressure (p), the temperature (T) and the enthalpy ($h = e + p/\rho$). We assume perfect gases, for which

$$p\left(\phi\right) = \rho R\left(\phi\right) T\left(\phi\right), \tag{3}$$

where $R(\phi) = Y_V R_V + Y_C R_C$, $R_V = R_u/m_V$, $R_C = R_u/m_C$, R_u is the universal gas constant and m_C and m_V are the molar weights of the carrier gas and vapor respectively. For the small temperature and pressure range to be simulated, the species heat capacities at constant pressure, $C_{p,C}$ and $C_{p,V}$, are assumed constant; then

$$h\left(\phi\right) = h_V Y_V + h_C Y_C = C_p\left(\phi\right) T\left(\phi\right) + h_V^0 Y_V, \tag{4}$$

$$e\left(\phi\right) = e_V Y_V + e_C Y_C = C_v\left(\phi\right) T\left(\phi\right) + h_V^0 Y_V, \tag{5}$$

where $C_p\left(\phi\right) = C_{p,V} Y_V + C_{p,C} Y_C$, $C_v = C_p - R$, and h_V^0 is the reference vapor enthalpy which accounts for the enthalpy difference between the vapor and carrier gas at the reference conditions (T^0, p^0).

For Eq. 2, the viscous stress σ_{ij}, the vapor mass flux j_{Vj} and the heat flux q_j are given by

$$\sigma_{ij}\left(\phi\right) = 2\mu\left(S_{ij} - \frac{1}{3}S_{kk}\delta_{ij}\right) \tag{6}$$

$$S_{ij}\left(\phi\right) = \frac{1}{2}\left(\frac{\partial u_i}{\partial x_j} + \frac{\partial u_j}{\partial x_i}\right) \tag{7}$$

$$\begin{aligned} j_{Vj}\left(\phi\right) = &-\rho D\frac{\partial Y_V}{\partial x_j} \\ &-\rho D\left(\frac{Y_V}{m_V} + \frac{Y_C}{m_C}\right)\left(m_C - m_V\right)\frac{Y_V Y_C}{p\left(\phi\right)}\frac{\partial p\left(\phi\right)}{\partial x_j} \end{aligned} \tag{8}$$

$$q_j\left(\phi\right) = -\lambda\frac{\partial T\left(\phi\right)}{\partial x_j} + \left[h_V\left(\phi\right) - h_C\left(\phi\right)\right] j_{Vj}\left(\phi\right), \tag{9}$$

where S_{ij} is the strain rate. The viscosity μ, the diffusion coefficient D and the thermal conductivity λ are assumed constant, and will be defined through the Prandtl and Schmidt numbers, $\mathrm{Pr} = \mu C_p/\lambda$ and $Sc = \mu/\left(\rho D\right)$.

2.2 Drop (liquid-phase) equations

We define $Z = \{X_i, v_i, T_d, m_d\}$ as the drop field with position X_i, velocity v_i, temperature T_d, and mass m_d. Under the assumptions stated previously, the evolution equations for the drops, in a Lagrangian frame, are:[6]

$$dZ/dt = \Sigma(\psi_f, \psi_s, Z), \tag{10}$$

$$\Sigma = \left\{v_i, \frac{F_i}{m_d}, \frac{Q + \dot{m}_d L_V\left(Z\right)}{m_d C_L}, \dot{m}_d\right\}, \tag{11}$$

where F_i is the drag force, Q is the heat flux, $\dot{m}_d$ is the evaporation rate, and C_L is the heat capacity of the drop liquid. L_V is the latent heat of vaporization, which, for calorically perfect gases, is a linear function of temperature, $L_V = h_V^0 - (C_L - C_{p,V})T_d$. The drop evolution depends on the gas-phase primitive variables, $\psi\left(\phi\right) = \{u_i, T, Y_V, p\}$, evaluated either at the drop surface (subscript s) or at the drop far-field (subscript f). The far-field variables are taken as the gas-phase primitive variables interpolated to the drop locations. The detailed expressions[6] for F_i, Q, and $\dot{m}_d$ involve validated correlations for point drops which are based on Stokes drag, with the particle time constant defined as[20] $\tau_d = \rho_L d^2/\left(18\mu\right)$, where ρ_L is the density of the liquid and d is the drop diameter (spherical drops; $m_d = \rho_L \pi d^3/6$):

$$F_i\left(\psi_f, Z\right) = \frac{m_d}{\tau_d} f_1 (u_{i,f} - v_i) \tag{12}$$

$$Q\left(\psi_f, Z\right) = \frac{m_d}{\tau_d}\frac{Nu}{3\,\mathrm{Pr}} C_{p,f} f_2 (T_f - T_d) \tag{13}$$

$$\dot{m}_d\left(\psi_f, \psi_s, Z\right) = -\frac{m_d}{\tau_d}\frac{Sh}{3Sc}\ln\left(1 + B_M\right) \tag{14}$$

Here, f_1 is an empirical correlation to correct the Stokes drag for finite drop Reynolds numbers and the mass transfer number is $B_M = (Y_{V,s} - Y_{V,f})/(1 - Y_{V,s})$. The Nusselt, Nu, and Sherwood, Sh, numbers are empirically modified for convective corrections to heat and mass transfer based on the Ranz-Marshall correlations. Except for τ_d, which depends on μ, Eqs. 12–14 depend essentially on ratios of transport properties through non-dimensional numbers. Therefore, the value of τ_d and thus for a given liquid and drop size, the value of μ determines the interaction time between drops and gas.

2.3 Source terms

Each drop acts as a point source[6] of mass, momentum and energy for the gas phase, with the drop source vector $S_d(\psi_f, \psi_s, Z) = \{S_{I,d}, S_{II,i,d}, S_{III,d}, S_{I,d}\}$

$$S_{I,d} = -\dot{m}_d,\ S_{II,i,d} = -\left[F_i + \dot{m}_d v_i\right],$$
$$S_{III,d} = -\left[F_i v_i + Q + \dot{m}_d\left(v_i v_i/2 + h_{V,s}\right)\right]. \quad (15)$$

The drop sources in the Lagrangian frame are reconstructed in the Eulerian frame to obtain the gas-phase source vector $S(\psi, Z)$ for Eq. 1 using

$$S(\psi, Z) = \sum_{\alpha=1}^{N_\alpha}\left(w_\alpha/V\right)\left[S_d(\psi_f, \psi_s, Z)\right]_\alpha \quad (16)$$

where the summation is over the N_α drops within the local numerical discretization volume V, and the geometrical weighting factor w_α distributes the individual drop contributions to the corners of V proportionally to the drop distance from those nodes.[6] These source terms are then minimally 'smoothed' using a conservative operator so as to retain numerical stability of the Eulerian gas-phase fields;[6] this smoothing is not a filter in that it does not remove flow scales, but is required for successful simulations due to the 'spottiness' of the source terms.

2.4 Flow configuration and numerical procedure

The mixing layer geometric configuration is illustrated in Fig. 1, where the streamwise (x_1), the cross-stream (x_2), and the spanwise (x_3) coordinates are shown. Periodic boundary conditions are used in the x_1 and x_3 directions, and adiabatic slip wall conditions[21] are employed for the x_2 boundaries. Drops reaching the slip walls are assumed to stick to the wall, but are otherwise transported according to Eq. 10. Initially, the gas phase consists only of the carrier gas (no vapor); the initial mean streamwise velocity has an error-function profile. To promote layer growth, the layer is initially perturbed so as to induce roll-up and pairing. The perturbations specify spanwise and streamwise vorticity fluctuations.[6,22] The evolution of the layer comprises two pairings for the four initial spanwise vortices to form a single vortex. The drops are initially distributed randomly throughout the $x_2 < 0$ domain; the initial velocity of each drop is the same as that of the gas phase at its location.

From the DNS,[8] we consider the cases with initial Reynolds number, $\mathrm{Re}_0 = \rho_0 \Delta U_0 \delta_{\omega,0}/\mu$, of 600 and with initial mass loading, ML_0, of 0.2 (case TP600a2) and 0.5 (case TP600a5), listed in Table 1. The initial number of drops $N_{d,0}$ is determined by ML_0. The initial vorticity thickness is $\delta_{\omega,0} = \delta_\omega(0)$ where $\delta_\omega(t) = \Delta U_0/\left(\partial\langle u_1\rangle/\partial x_2\right)_{\max}$; the brackets $\langle\rangle$ denote averaging over homogeneous (x_1, x_3) planes, $\Delta U_0 = 2U_0$ is the velocity difference across the layer and ρ_0 is the initial gas density. For the cases considered, ρ_0=0.9415 kg/m^3, ΔU_0=271.69m/s, $\delta_{\omega,0}$=6.859$\times$10^{-3}m and the convective Mach number, $M_{c,0}$, is 0.35. The domain size is 0.2m$\times$0.22m$\times$0.12m and the grid resolution is 288$\times$320$\times$176 points. The adequacy of the resolution was assessed by computing one-dimensional energy spectra at the transitional times; these plots showed that most of the energy is in the large scales and that there was no accumulation of energy in the small scales. At the transition times listed in Table 1, the momentum thickness δ_m is 2.627 and 2.613 for TP600a2 and TP600a5, respectively.

All thermophysical properties are based on air as the carrier gas and n-decane as the drop liquid[7] (m_C = 28.97, m_V = 142, Pr=Sc=0.697, ρ_L=642kg/m^3). Initially, all the drops have the same temperature (345K), which is lower than the initial gas-phase temperature (375K) and the liquid boiling temperature (447.7 K) to promote evaporation. The drop size distribution is specified through the drop Stokes number $St = \tau_d \Delta U_0/\delta_{\omega,0} = d^2\left(\rho_L \Delta U_0\right)/\left(18\mu\delta_{\omega,0}\right)$. In the present study, ρ_L and μ are constant, therefore St is linearly proportional to the drop diameter squared. St initially has a Gaussian distribution with mean 3 and standard deviation 0.5. Evaporation causes a reduction in the drop size and any drop diminishing to $St \leq 0.1$ is removed from the domain.

Equations 1 and 10 are solved numerically using a fourth-order explicit Runge-Kutta temporal integration for time derivatives and an eighth-order central finite differencing with tenth-order filtering for spatial derivatives;[23] this filtering introduces a small amount of dissipation that serves only to stabilize the computations for long-time integrations. A fourth-order Lagrange interpolation procedure is used to obtain gas-phase variable values at the drop locations.[6]

3 LES Methodology

The LES uses the same mathematical description as the DNS, i.e. Eulerian for the gas phase and Lagrangian for the liquid phase. The LES gas-phase equations are derived by spatially filtering the gas-phase DNS equations (1), and then making various simplifying assumptions.[8] The filtering operation is defined as:

$$\bar{\psi}(\vec{x}) = \int_{V_f} \psi(\vec{y})\, G(\vec{x} - \vec{y})\, d\vec{y} \quad (17)$$

where G is the filter function and V_f is the filtering volume. The present finite-difference computations use a top-hat filter; so $\bar{\psi}$ is simply the volume-average. The Favre (density-weighted) filtering is defined as $\tilde{\psi} = \overline{\rho\psi}/\bar{\rho}$. It is assumed that filtering and differentiation commute, which is true except near boundaries (because the size of the filtering volume decreases as the boundary is approached).

The LES uses N_{cd} computational drops to represent the N_d physical drops, that is each computational drop represents $N_R \equiv N_d/N_{cd}$ physical drops. The LES computational drops, denoted $\bar{Z}$, follow the DNS evolution equations (10):

$$d\bar{Z}/dt = \Sigma(\tilde{\psi}_f, \tilde{\psi}_s, \bar{Z}), \tag{18}$$

where Σ has the same functional form as in the DNS but is based on $\tilde{\psi}$ and $\bar{Z}$ instead of ψ and Z.

3.1 Gas phase LES equations

The gas-phase LES equations are:[8]

$$\frac{\partial\bar{\phi}}{\partial t} + \frac{\partial\left(\bar{\phi}\tilde{u}_j\right)}{\partial x_j} = \frac{\partial}{\partial x_j}\left[\Theta_j(\bar{\phi}) + \Theta_{SGS,j}\right] + \bar{S}, \tag{19}$$

$$\Theta_{SGS,j} = \left\{0, -\bar{\rho}\tau_{ij}, \left(-\bar{\rho}\zeta_j - \bar{\rho}\tau_{ij}\tilde{u}_i\right), -\bar{\rho}\eta_j\right\};$$

where $\bar{\phi}$ denotes the filtered flow field, $\bar{S} = \left\{\bar{S}_I, \bar{S}_{II,i}, \bar{S}_{III}, \bar{S}_I\right\}$ are the filtered source terms (FSTs), Θ_j has the same form as the DNS (Eq. 2) but is computed on the filtered flow field, and the SGS fluxes are

$$\tau_{ij} = \widetilde{u_i u_j} - \tilde{u}_i\tilde{u}_j, \zeta_j = \widetilde{hu_j} - \tilde{h}\tilde{u}_j, \eta_j = \widetilde{Y_V u_j} - \tilde{Y}_V\tilde{u}_j. \tag{20}$$

These equations are based on validated assumptions,[8] that

$$\tfrac{1}{2}\left(\overline{\rho u_i u_i u_j} - \overline{\rho u_i u_i}\tilde{u}_j\right) = \bar{\rho}\tau_{ij}\tilde{u}_i, \tag{21}$$

and that $\overline{f(\phi)} = f\left(\bar{\phi}\right)$ i.e.

$$\begin{aligned} &\tilde{e} = e\left(\bar{\phi}\right), \quad \overline{T} = T\left(\bar{\phi}\right), \quad \widetilde{T} = T\left(\bar{\phi}\right), \quad \bar{p} = p\left(\bar{\phi}\right), \\ &\tilde{h} = h\left(\bar{\phi}\right), \quad \tilde{q}_j = q_j\left(\bar{\phi}\right), \quad \tilde{j}_{Vj} = j_{Vj}\left(\bar{\phi}\right), \\ &\bar{\sigma}_{ij} = \sigma_{ij}\left(\bar{\phi}\right), \quad \overline{u_i\sigma_{ij}} = \tilde{u}_i\sigma_{ij}\left(\bar{\phi}\right), \end{aligned} \tag{22}$$

where the listed functions have the same form as in the DNS. Equation 19 for $\bar{\phi}$ contains terms that cannot be computed directly from $\bar{\phi}$ and that therefore need to be modeled, namely, (1) the FSTs and (2) the SGS fluxes.

3.2 Models for filtered source terms

From Eq. 17, the FSTs are properly interpreted by considering a drop located at $\vec{X}$ within the filtering volume V_f and its contribution within that volume

$$\bar{S}\left(\vec{x}\right) = \int_{V_f} S_d\delta(\vec{y} - \vec{X})G\left(\vec{x} - \vec{y}\right)d\vec{y}, \tag{23}$$

where $S_d\delta(\vec{y}-\vec{X})$ is the point-source contribution from the drop and δ is the delta function. When G is a top-hat filter, the exact FSTs are

$$\bar{S} = (1/V_f)\sum_{\alpha=1}^{N_\alpha}\left[S_d\left(\psi, Z\right)\right]_\alpha, \tag{24}$$

a volume-average over the N_α physical drops within the filtering volume V_f, where S_d was defined in Eq. 15. The FSTs are modeled from $\bar{\phi}$ and $\bar{Z}$ as[8]

$$\bar{S} = N_R\sum_{\beta=1}^{N_\beta}\left(1/V_f\right)\left[S_d\left(\tilde{\psi}\left(\bar{\phi}\right), \bar{Z}\left(N_R\right)\right)\right]_\beta, \tag{25}$$

where the summation is over the N_β computational drops within the filtering volume V_f, and S_d has the same functional form as in the DNS (Eq. 15) with $\tilde{\psi}$ being the model for ψ, that is without modeling direct SGS effects on drop evolution. On an *a priori* basis, the model devoid of direct SGS effects on drop evolution proved almost as good as a model accounting deterministically for direct SGS effects and superior to a model accounting statistically for such effects.[8]

3.3 Subgrid-scale flux models

For compactness of notation, we denote the SGS fluxes for a variable φ as

$$\theta_j\left(\varphi\right) = \left(\widetilde{\varphi u_j} - \tilde{\varphi}\tilde{u}_j\right) \tag{26}$$

where $\theta_j\left(u_i\right) = \tau_{ij}$, $\theta_j\left(Y_V\right) = \eta_j$ and $\theta_j\left(h\right) = \zeta_j$. The model for $\theta_j\left(\varphi\right)$, to be calculated on the filtered flow field $\left(\bar{\phi}\right)$, is denoted $\mu_j\left(\tilde{\varphi};\bar{\phi},\bar{\Delta}\right)$ (associated with the filter width $\bar{\Delta}$ and with the velocity $\tilde{u}_j$); μ_j does not contain the model coefficient. For the SGS fluxes defined in Eq. 20, we consider here the three typical SGS models: The Smagorinsky[24] (SM) model combined with the Yoshizawa[25] (YO) model is

$$\begin{aligned} \theta_j\left(u_i\right) &= C_{SM}\mu_j\left(\tilde{u}_i\right) + C_{YO}\mu\delta_{ij}/3 \\ \mu\left(\bar{\phi},\bar{\Delta}\right) &= \bar{\Delta}^2 S^2\left(\bar{\phi}\right) \\ \mu_j\left(\tilde{u}_i;\bar{\phi},\bar{\Delta}\right) &= -\bar{\Delta}^2 S\left(\bar{\phi}\right)\left[S_{ij}\left(\bar{\phi}\right) - S_{kk}\left(\bar{\phi}\right)\delta_{ij}/3\right] \end{aligned} \tag{27}$$

$$\begin{aligned} \theta_j\left(\varphi\right) &= C_{SM}\mu_j\left(\tilde{\varphi}\right); \varphi = Y_V, h \\ \mu_j\left(\tilde{\varphi};\bar{\phi},\bar{\Delta}\right) &= -\bar{\Delta}^2 S\left(\bar{\phi}\right)\frac{1}{2}\frac{\partial\tilde{\varphi}}{\partial x_j} \end{aligned} \tag{28}$$

where $S^2 = S_{ij}S_{ij}$. The Gradient (GR) model is[26]

$$\begin{aligned} \theta_j\left(\varphi\right) &= C_{GR}\mu_j\left(\tilde{\varphi}\right) \\ \mu_j\left(\tilde{\varphi};\bar{\phi},\bar{\Delta}\right) &= \bar{\Delta}^2\frac{\partial\tilde{\varphi}}{\partial x_k}\frac{\partial\tilde{u}_j}{\partial x_k}; \varphi = u_i, Y_V, h \end{aligned} \tag{29}$$

The Scale-Similarity (SS) model is[27]

$$\begin{aligned} \theta_j\left(\varphi\right) &= C_{SS}\mu_j\left(\tilde{\varphi}\right) \\ \mu_j\left(\tilde{\varphi};\bar{\phi},\bar{\Delta}\right) &= \left(\widehat{\tilde{\varphi}\tilde{u}_j} - \hat{\tilde{\varphi}}\hat{\tilde{u}}_j\right); \varphi = u_i, Y_V, h \end{aligned} \tag{30}$$

where the overhat $(\hat{\ })$ denotes (unweighted) filtering at the test-filter level $\hat{\Delta} \geq \bar{\Delta}$.

For the SS model, we used the DNS-calibrated constant-coefficient value[8] of $C_{SS} = 1.996$ (model denoted SSC; $\hat{\Delta} = \bar{\Delta}$). For the GR and SM models, the calibrated constant-coefficients,[8] while adequate for SP flows were not consistently stable for TP flows. Therefore, we turned to dynamic Smagorinsky (SMD) and Gradient (GRD) models, where the coefficients are dynamically computed as part of the LES solution. Basically, dynamic modeling attempts to deduce the SGS behavior from that of the smallest resolved scales. The essence of the method is to relate the grid-level SGS flux, θ_j, and the test-level SGS flux,

$$T_j(\varphi) = \left(\widehat{\widetilde{\varphi u_j}} - \widehat{\tilde{\varphi}}\widehat{\tilde{u}}_j\right), \tag{31}$$

to the test-level resolved flux, L_j, through the Germano identity:[28]

$$L_j(\varphi) \equiv \widehat{\tilde{\varphi}\tilde{u}_j} - \widehat{\tilde{\varphi}}\widehat{\tilde{u}}_j = T_j - \hat{\theta}_j. \tag{32}$$

Using a T_j model having the same functional from as the θ_j model but based on $\widehat{\tilde{\varphi}}$ and $\widehat{\bar{\Delta}}$ (instead of $\tilde{\varphi}$ and $\bar{\Delta}$), the L_j model is

$$M_j(\varphi) = \mu_j(\widehat{\tilde{\varphi}}) - \widehat{\mu_j(\tilde{\varphi})}. \tag{33}$$

The filter width $\widehat{\bar{\Delta}}$, due to the re-filtering, is $\widehat{\bar{\Delta}}^2 = \bar{\Delta}^2 + \hat{\Delta}^2$ for the top-hat filter.[29]

The model coefficient, valid for the entire domain, can be extracted using a least-squares fit,[30]

$$C(\varphi) = \frac{\langle\langle L_j(\varphi) M_j(\varphi)\rangle\rangle}{\langle\langle M_k(\varphi) M_k(\varphi)\rangle\rangle}, \tag{34}$$

where $\langle\langle\rangle\rangle$ denotes averaging over the entire domain; the coefficient can also be computed on homogeneous planes by replacing the domain averaging with plane averaging. The coefficients were obtained using domain averaging for τ_{ij}, domain or homogeneous-plane averaging for ζ_j (respectively for the SMD or GRD model) and homogeneous-plane averaging for η_j. These averagings were consistently stable for SP and TP flows. All the dynamic models use $\hat{\Delta} = 2\bar{\Delta}$. We use three coefficients for SMD (for τ_{ij}, ζ_j and η_j) and four for GRD (for $\tau_{ij,i=j}$,$\tau_{ij,i\neq j}$, ζ_j and η_j). (The use of dimensional variables in the present formulation necessitates the separate computation of the coefficient for each type of SGS flux.) In view of our observations[8] that the Scale-Similarity and Gradient models have much better correlations with the SGS fluxes than does the Smagorinsky model, we do not consider 'mixed' models, in which the (dynamic) Smagorinsky model is used to add dissipation to the other two models.

3.4 Initial conditions and numerical procedure

The LES results will be compared to the FC-DNS, that is the DNS field which has been filtered and coarsened so that only the DNS grid points corresponding to the LES grid are used, and with N_{cd} physical drops selected from the array of N_d physical drops using a stride of N_R. Therefore, it is appropriate to use the FC-DNS initial condition. The type of LES filter, in this case a cubic top-hat filter, explicitly appears in computing the initial condition, and also during the LES when computing the SGS fluxes (if the similarity or a dynamic SGS model is used) and the FSTs. The DNS cases being considered here are listed in Table 1; the corresponding LES cases are listed in Table 2. The LES grid is coarser than the DNS grid, with $\Delta x_{LES} = 4\Delta x_{DNS}$ ($72\times80\times44$ points) and $\bar{\Delta} = 2\Delta x_{LES}$; also, N_R=8. The LES are performed using the same numerical scheme as the DNS (see Section 2.4). Most of the analysis is performed at the DNS transitional times listed in Table 1. Since all the LES use the same FST model, they will be identified according to the SGS-flux model as GRD, SMD or SSC LES.

At the DNS transition time, the FC-DNS δ_m is almost the same as the DNS (within 0.2%) but the LES δ_m are 11% to 15% lower than the DNS value, with the SSC (GRD) being closest to the DNS for TP600a2 (TP600a5). The LES have approximately the same total number of drops as the FC-DNS (98%–100%), however they have too many (SMD; 105%–115%) or too few (GRD, SSC; 75%-91%) drops within the layer, with the layer edge planes defined where $\langle u_1\rangle$ is 1% of the free stream values. Given the considerably lower CPU requirements for LES compared to DNS (up to a factor of 120 shorter CPU time), the interest is whether the detailed characteristics of the layer are accurately predicted by LES.

4 Detailed Characteristics

4.1 Dynamic Characteristics

To assess the quality of LES in predicting the dynamic characteristics, illustrated in Fig. 2 are the time-evolution of the enstrophy $\langle\langle\omega\cdot\omega\rangle\rangle$, a measure of stretching and tilting which promotes the generation of turbulence. For convenience, the bar and tilde that denote filtered quantities are omitted; all quantities are computed from the filtered flow field quantities. $\langle\langle\omega\cdot\omega\rangle\rangle$ increases dramatically at roll up, then grows steadily, with a slight dip for TP600a2 at the first pairing, culminates shortly after the second pairing, and afterwards declines. Considering the LES, the SMD model has much less vorticity generation than the FC-DNS, with only a slight increase during the layer evolution. In contrast, both the GRD and SSC model qualitatively mimic the FC-DNS $\langle\langle\omega\cdot\omega\rangle\rangle$ evolution, with the GRD being a better quantitative match. Both GRD and SSC peak at a lower value and at an earlier time that the FC-DNS; however the GRD is closer to the FC-DNS. The indications are that the SMD model has much less small-scale activity and generation than the other two LES models.

The local enstrophy in the between-the-braid plane ($x_3/\delta_{\omega,0}$=8.75) is plotted in Fig. 3, for the TP600a2 FC-DNS and LES at the DNS transition time, $t^* = 105$ (results for TP600a5 are similar). The contour levels are from 10% to 90% of the maximum value of $\omega \cdot \omega$ in the plane. The FC-DNS shows substantial small-scale activity, well-distributed within the ultimate vortex that results from the pairing of the four initial spanwise vortices. The SMD LES displays only enstrophy associated with the largest-scale vortex and none associated with small scale structures, confirming the indications of the global measures in Fig. 2 that the SMD has little generation of small scale structures. Furthermore, as in the global measures, the SMD enstrophy level is much lower than the FC-DNS. The GRD and SSC models show small scale structures within the ultimate vortex, similar to the FC-DNS; however, fewer structures are observed, due to the lower resolution of the LES compared to the DNS. In this plane, the FC-DNS range of values is better matched by the SSC than by the GRD, although the size and distribution of small structures of the GRD more resembles the FC-DNS than does the SSC.

The enstrophy generation at the DNS transition time is analyzed by means of the budget:

$$\begin{aligned} D(\omega\cdot\omega)/Dt = {} & 2\omega\cdot[(\omega\cdot\nabla)\,\mathbf{u}] - 2(\omega\cdot\omega)(\nabla\cdot\mathbf{u}) \\ & + 2\omega\cdot\{\nabla\times[(-\nabla p+\nabla\cdot\sigma)/\rho]\} \\ & + 2\omega\cdot\{\nabla\times[(\mathbf{S}_{II}-\mathbf{u}S_I)/\rho]\} \end{aligned} \tag{35}$$

Averages in homogenous planes of $D(\omega\cdot\omega)/Dt$, plotted in Fig. 4 for TP600a2 and TP600a5, show for TP600a2 approximately the same total $D(\omega\cdot\omega)/Dt$ for all LES, which compares well to the FC-DNS. For TP600a5, the results are similar, although the SSC model has smaller magnitude of $D(\omega\cdot\omega)/Dt$ than the other LES. All LES models seem to capture the spatial extent of vorticity activity, signifying that the extent is mainly governed by the large-scale structure, independent of the SGS model. However, differences emerge in the relative contributions of the six terms in Eq. 35, plotted in Fig. 5 for TP600a2 FC-DNS and LES. All models follow the FC-DNS in that the stretching/tilting term has the largest magnitude of terms that are on average positive, while the viscous term has the largest magnitude of negative terms. Closer examination of the SMD results shows an overall lower magnitude of stretching/tilting and viscous terms compared to the FC-DNS, while having a larger magnitude of source terms. Also, the SMD has a dip in the stretching/tilting term in the upper stream.

The assessment of the dynamic characteristics of the LES is that the SMD model does not capture small scale activity, while the GRD and SSC models do. Large scale activity, such as the extent of the ultimate vortex, appears to be independent of the SGS model, and thus is captured by all LES.

4.2 Mixing Characteristics

We now turn to an assessment of the LES mixing characteristics. Together, the temperature and equivalence ratio determine the propensity for combustion. The equivalence ratio is defined as

$$\Phi = \frac{(M_F/M_O)}{(M_F/M_O)_{st}} \tag{36}$$

where M_F and M_O denote the mass of the fuel and oxidizer respectively, and st indicates the stoichiometric conditions. Then the local and global equivalence ratios can be computed as

$$\Phi = \frac{(Y_V/Y_C)}{(Y_V/Y_C)_{st}},\ \Phi_g = \frac{(M_V/M_C)}{(M_V/M_C)_{st}} \tag{37}$$

where M_V and M_C are the total mass of vapor and carrier gas, respectively, in the domain. For the air-decane reaction, $C_{10}H_{22}+15.5(O_2+3.76N_2) \rightarrow 10CO_2+11H_2O+58.28N_2$,

$$\left(\frac{M_F}{M_O}\right)_{st} = \left(\frac{Y_V}{Y_C}\right)_{st} = \frac{1\,(142)}{15.5(28.97)} = 0.316$$

To assess the species mixing, the evolution of the global equivalence ratio is depicted in Fig. 6, for both TP600a2 and TP600a5. All LES show good agreement with the FC-DNS, and thus have the proper global amount of drop evaporation, suggesting that in this flow configuration the global evaporation is mainly driven by large scale structures. The local equivalence ratio is plotted in Fig. 7, for TP600a2 in the between-the-braid plane. The contour plots in Fig. 7 show that all models do well in capturing the range of values of Φ. However, the SMD model does not show appropriate small scale activity, while the GRD and SSC do.

The temperature is plotted in Fig. 8, also for TP600a2 in the between-the-braid plane. The temperature variation observed in the FC-DNS is mainly due to the cooling effect of the drops, which have reduced the carrier gas from 375K. In the lower stream, the temperature has fallen below the initial drop temperature of 340K, as some of the energy in the system has been utilized by phase change. In addition to the large scale temperature variation, most noticeable in the cross-stream direction, there are small scale variations, on the order of small scale structures observed in $\omega\cdot\omega$ (Fig. 3). Comparing the FC-DNS to the LES, it is clear that the SMD model, as in the dynamics, does not capture the small scale variations. Also, the SMD temperature range exceeds that of the FC-DNS. The SSC model best matches the FC-DNS temperature range, while the GRD leads to a slightly colder flow field. Both the GRD and SSC show the small scale variations observed in the FC-DNS.

In view of the poor local performance of the SMD model, global results have to be interpreted with caution when used as indicators of small-scale or turbulence activity. Since it is the local thermodynamic

state that governs combustions, the poor local predictions of the SMD model seem to disqualify it from combustion applications.

4.3 Drop distribution

The LES do not incorporate direct SGS effects on the drops, but SGS effects enter indirectly in affecting the resolved flow field that is felt by the drops. Here the emphasis is in whether the LES preserve the relation between dynamics and drop locations.

The drop-number density, $\rho_n = N_R\,(N_\beta/V_f)$ where N_β is the number of computational drops in the filtering volume V_f, is plotted in Fig. 9, for TP600a2 in the between-the-braid plane. The drops in the SMD are incorrectly located, being concentrated on the edges of the ultimate vortex, rather that within it. The GRD and SSC drops, on the other hand, are distributed similarly to the FC-DNS, with voids corresponding to high vorticity regions (see Fig. 3), although their maximum ρ_n is about 30% lower. In Fig. 10 are shown the number of drops within the layer versus St for the FC-DNS and the LES. The range of St values and the St with the largest number of drops seem well predicted by all models. However, the TP600a2 (TP600a5) SMD has too many drops for St >0.7 (1.7). The TP600a2 (TP600a5) GRD and SSC have too few drops for St >0.9 (1.4) and St >1.1 (1.4), respectively.

Next, we plot the drop distribution conditioned on the second invariant of the deformation

$$I_2\,(\mathbf{D}) = -S_{ij}S_{ij}/2 + S_{ii}S_{jj}/2 + \omega_i\omega_i/4 \qquad (38)$$

where $D_{ij} = \partial u_i/\partial x_j$. For these layers, $S_{ii}S_{jj}/2$ is much smaller than the other terms, so regions of negative $I_2\,(\mathbf{D})$ are strain-dominated, while regions of positive $I_2\,(\mathbf{D})$ are vorticity-dominated. The number of drops with particular values of $I_2\,(\mathbf{D})$ is plotted in Fig. 11; the value of $I_2\,(\mathbf{D})$ associated with each drop is obtained by interpolating $I_2\,(\mathbf{D})$ from the grid points to the drop locations, using fourth-order Lagrangian interpolation. Qualitatively, all LES match the DNS in that drops are most likely to be in regions of $I_2\,(\mathbf{D}) \simeq 0$. However, the number of drops is reduced for all LES when compared to the FC-DNS. For TP600a5, the reduction is consistent whether $I_2\,(\mathbf{D})$ is positive or negative, with the GRD best matching the FC-DNS, followed by the SSC and worst agreement from the SMD. For TP600a2, the worst result still comes from the SMD model, but the GRD and SSC models now perform comparably, and on the positive $I_2\,(\mathbf{D})$ side match the FC-DNS very well. The lower mass loading leads to less vapor saturation and more evaporation and thus smaller drops for the TP600a2; these drops tend to better follow the flow than the larger TP600a5 drops and are therefore less susceptible to modeling errors.

The drop number density is plotted in Fig. 12, conditionally domain-averaged on $I_2\,(\mathbf{D})$. The FC-DNS ρ_n average is highest for $I_2\,(\mathbf{D}) \simeq 0$, followed by $I_2\,(\mathbf{D}) < 0$, and lowest for $I_2\,(\mathbf{D}) > 0$. The GRD model best matches the FC-DNS curve, with good agreement throughout the $I_2\,(\mathbf{D})$ range. At the other extreme, the SMD model has a truncated $I_2\,(\mathbf{D})$ range, particularly on the negative side, with the highest number density for $I_2\,(\mathbf{D})\,(\delta_{\omega,0}/\Delta U_0)^2 \simeq -0.022$; both the location and magnitude of the ρ_n peak differ markedly from the FC-DNS. The SSC model, while not as good as the GRD, is much better than the SMD, although for TP600a2 (TP600a5) it overpredicts (underpredicts) the ρ_n average for $I_2\,(\mathbf{D}) < 0$.

Therefore, consistent with the global evaporation results (Fig. 6), the range of drop sizes is well predicted by all SGS models. However, the flow field, especially the small scale structures, is not well predicted by the SMD model, and moreover it does not predict the correct relation between flow structures and drop distributions. This serves as further confirmation of the superiority of the GRD and SSC models over the SMD model.

4.4 Irreversible entropy production

The irreversible entropy production is the dissipation, which is of crucial importance in determining the characteristics of turbulent flows because it contains the viscous dissipation which measures the loss of mechanical energy to heat and the scalar dissipation which manifests in the mixing, as well as dissipation due to temperature gradients and due to drop source terms. The effect of the LES dynamic, mixing and drop distribution characteristics on duplicating the FC-DNS dissipation is here addressed. From the entropy equation,[31] we have derived the rate of irreversible entropy production as:[8]

$$\begin{aligned} g &= g_{III} + g_{II} + g_{I,kine} + g_{I,chpot} \\ &\quad + g_{visc} + g_{temp} + g_{mass} \end{aligned} \qquad (39)$$

$$\begin{aligned} g_{III} &= \frac{S_{III}}{T}, \quad g_{II} = -u_i\frac{S_{II,i}}{T}, \\ g_{I,kine} &= \left(\tfrac{1}{2}u_iu_i\right)\frac{S_I}{T}, \quad g_{I,chpot} = -\mu_V\frac{S_I}{T}, \\ g_{visc} &= \frac{2\mu}{T}\left(S_{ij} - \frac{1}{3}S_{kk}\delta_{ij}\right)^2, \; g_{temp} = \frac{\lambda}{T^2}\frac{\partial T}{\partial x_j}\frac{\partial T}{\partial x_j}, \\ g_{mass} &= \frac{R_CR_V}{Y_CY_V\left(R_VY_V + R_CY_C\right)}\frac{j_{Vj}j_{Vj}}{\rho D} \end{aligned} \qquad (40)$$

where μ_V is the chemical potential of the vapor; $\mu_V = h_V - Ts_V$. The pure vapor entropy, s_V, is here calculated as

$$s_V = s_V^0 + C_{p,V}\ln\left(T/T^0\right) - R_V\ln\left(p/p^0\right), \qquad (41)$$

where s_V^0 is the reference entropy at $(T^0,\ p^0)$, obtained from integration or tables. Inspection of Eq. 39 shows that the gas-phase dissipation has several origins. First, the drops are energy, momentum and

mass sources with the resulting dissipation embodied in g_{III}, g_{II}, $g_{I,kine}$ and $g_{I,chpot}$. Note that $g_{I,kine}$ and $g_{I,chpot}$ are entirely due to evaporation, with $g_{I,kine}$ due to the gas-phase kinetic energy of the mass evolving from the drops, whereas $g_{I,chpot}$ is due to its chemical potential. Similar effects are contained in g_{III} and g_{II}, but these terms additionally have non-evaporation contributions from the drag on and the heating of the drops. The terms g_{visc}, g_{temp} and g_{mass} contain the flux-related dissipation and are positive semi-definite.

The terms in Eq. 39 are listed in Table 3, which contains the domain average and RMS values for TP600a2 and TP600a5 at transition, in decreasing order of FC-DNS RMS. Due to extreme sensitivity of g_{mass} to numerical error, the present results limit $|\partial(\ln Y_V)/\partial x_i| < 2/\Delta x_i$. Considering first the FC-DNS, the largest terms on average are g_{III}, which is positive, and $g_{I,chpot}$, which is negative and also of smaller magnitude. The g_{II} is also negative on average; its magnitude is larger than that of g_{visc} for TP600a5 FC-DNS but smaller than g_{visc} for TP600a2 FC-DNS. For both TP600a2 and TP600a5, g_{visc} and g_{II} are one to two orders of magnitude smaller than the largest terms. The smallest term is g_{temp}; of the two remaining terms (g_{mass} and $g_{I,kine}$), g_{mass} is minimally larger for TP600a2 while $g_{I,kine}$ is larger for TP600a5. For the FC-DNS RMS, TP600a2 and TP600a5 have the same ordering of terms: the largest magnitude term is g_{III}, followed by $g_{I,chpot}$, then g_{II}. Next are the flux-related terms, with g_{visc} being largest and g_{temp} being smallest; the remaining source-related term $g_{I,kine}$ has an RMS larger than g_{temp} but smaller than g_{mass}.

Comparing the LES with the FC-DNS, all LES preserve the ordering of terms of the FC-DNS RMS. Generally, the ordering of terms is also preserved for the average; however, g_{II} has the wrong sign for the TP600a2 SMD LES and for all TP600a5 LES, and the relative magnitudes of the $g_{I,kine}$ and g_{mass} averages are reversed for TP600a2 SMD, TP600a5 GRD and TP600a5 SSC. Thus, g_{II} and g_{mass} seem most sensitive to the LES modeling errors. The proportional contribution of all terms to the total is generally the same for the LES and the FC-DNS, however, the magnitude of the LES terms varies considerably from the FC-DNS. In particular, the average g for the LES is lower than the FC-DNS, being about 50%-60% for GRD and SSC and about 75% for SMD; the largest magnitude terms, g_{III} and $g_{I,chpot}$, are typically even lower, 30%-50% for GRD and SSC and 60%-75% for the SMD.

Since the dissipation is dominated by source-term contributions and, as already discussed, the global amount of evaporation is well-predicted by all models, the global dissipation results are generally insensitive to the choice of SGS model. This finding explains previous success of other researchers with the SMD model,[9,13] as it better predicts the global amount of dissipation compared to the GRD and SSC models. However, the location of the dissipation predicted by the SMD LES is not correct, as seen on the contour plots in Fig. 13. As previously observed for other quantities (Figs. 3, 7 and 8), the SMD model is devoid of small scale structure, while the GRD and SSC have similar small-scale structure to the FC-DNS. Because g is dominated by source terms, which result from the drop locations (Fig. 9), the SGS model does affect the local dissipation distribution. The range of g values is larger for the SMD model than for the FC-DNS, while the range is smaller for the GRD and SSC. The implication is that the SMD has less spatial extent but more intensity of high dissipation regions coinciding with the overly high drop accumulation, leading in the present cases to global average dissipation that is comparable to that of the other LES models.

5 Conclusions

DNS and LES of a temporal mixing layer with evaporating drops have been compared in order to assess the ability of the LES to replicate detailed aspects of the DNS. The LES were conducted with models for the filtered source terms and the SGS fluxes. Three different SGS-flux models were evaluated: dynamic Gradient (GRD), dynamic Smagorinsky (SMD) and constant-coefficient Scale-Similarity (SSC). The dynamic models used model coefficients that were computed during LES from the LES solution, while the SSC model used a constant-coefficient value calibrated on the DNS database. The LES used a reduced computational drop field, with each LES drop representing eight physical DNS drops, as well as reduced flow-field resolution, with the LES grid spacing being four times that of the DNS. All LES captured the largest scale vortex, and processes associated with it, such as the global fuel-to-vapor ratio and the range of drop sizes. A comparison of the dynamic and mixing characteristics revealed the inability of the SMD model to replicate small-scale structures, in both dynamic (enstrophy) and thermodynamic (temperature, equivalence ratio) characteristics. The GRD and SSC model did capture such small-scale activity.

Although the LES did not directly incorporate SGS effects on drop evolution, the choice of SGS model was found to affect the drop spatial distribution. The relationship between drop spatial distribution and layer dynamics was explored by conditionally averaging on the second invariant of the deformation tensor. The GRD and SSC drop spatial distribution well matched the FC-DNS, with drops most likely to be located where the invariant was close to zero. The SMD model led to a different drop spatial distribution, with the correlation of invariant and drops being qualitatively different from the FC-DNS. The impact of layer dynamics, mixing and drop distribution on the irre-

versible entropy production (dissipation) was that all LES underpredict the global amount of dissipation. Although the SMD LES best predicts the global dissipation, it proved locally inaccurate, with the spatial distribution of dissipation being better matched by the GRD and the SSC. The dissipation activity is mainly due to drop source terms.

The overall assessment is that while the SMD model does capture some global aspects, local detailed aspects are better predicted by the GRD and SSC models. Therefore the GRD and SSC models are recommended for situations, such as combustion, where the local conditions have a significant impact on the flow. The GRD model has the advantage over the SSC model of not requiring a calibrated coefficient. Future work includes incorporating direct SGS effects on the drops[8] to potentially improve the LES results.

Acknowledgements

This work was conducted at the Jet Propulsion Laboratory (JPL) of the California Institute of Technology (Caltech) under the sponsorship of the U.S. Department of Energy, with R. Danz and D. Hooker serving as contract monitors, under an agreement with the National Aeronautics and Space Administration. Computations were performed on the SGI Origin 2000 at the JPL Supercomputing Center.

References

[1]M. Boivin, O. Simonin, and K.D. Squires. Direct numerical simulation of turbulence modulation by particles in isotropic turbulence. *Journal of Fluid Mechanics*, 375:235–263, 1998.

[2]F. Mashayek and F.A. Jaberi. Particle dispersion in forced isotropic low-Mach-number turbulence. *International Journal of Heat and Mass Transfer*, 42:2823–2836, 1999.

[3]F. Mashayek. Direct numerical simulations of evaporating droplet dispersion in forced low-Mach-number turbulence. *International Journal of Heat and Mass Transfer*, 41(17):2601–2617, 1998.

[4]J. Réveillon and L. Vervisch. Spray vaporization in nonpremixed turbulent combustion modeling: A single drop model. *Combustion and Flame*, 121:75–90, 2000.

[5]F. Mashayek. Droplet-turbulence interactions in low-Mach-number homogeneous shear two-phase flows. *Journal of Fluid Mechanics*, 367:163–203, 1998.

[6]R.S. Miller and J. Bellan. Direct numerical simulation of a confined three-dimensional gas mixing layer with one evaporating hydrocarbon-droplet laden stream. *Journal of Fluid Mechanics*, 384:293–338, 1999.

[7]R.S. Miller and J. Bellan. Direct numerical simulation and subgrid analysis of a transitional droplet laden mixing layer. *Physics of Fluids*, 12(3):650–671, March 2000.

[8]N. Okong'o and J. Bellan. Consistent large eddy simulation of a temporal mixing layer laden with evaporating drops. Part 1: Direct numerical simulation, formulation and *a priori* analysis. 2003. Accepted for publication in Journal of Fluid Mechanics.

[9]M. Boivin, O. Simonin, and K.D. Squires. On the prediction of gas-solid flows with two-way coupling using large eddy simulation. *Physics of Fluids*, 12(8):2080–2090, 2000.

[10]E. Deutsch and O. Simonin. Large eddy simulation applied to the modelling of particulate transport coefficients in turbulent two-phase flows. In *Eighth Symposium on Turbulent Shear Flows*, pages 10–1:1–6, September 1991.

[11]O. Simonin, E. Deutsch, and M. Boivin. Large eddy simulation and second-moment closure of particle fluctuating motion in two-phase turbulent shear flows. *Turbulent Shear Flows*, 9:85–115, 1993.

[12]W. Uijttewaal and R. Oliemans. Particle dispersion and deposition in direct numerical and large eddy simulations of vertical pipe flows. *Physics of Fluids*, 8(10):2590–2604, 1996.

[13]Q. Wang and K.D. Squires. Large eddy simulations of particle-laden turbulent channel flow. *Physics of Fluids*, 8(5):1207–1223, 1996.

[14]Y. Yamamoto, M. Potthoff, T. Tanaka, T. Kajishima, and Y. Tsuji. Large-eddy simulation of turbulent gas-particle flow in a vertical channel: Effect of considering inter-particle collisions. *Journal of Fluid Mechanics*, 442:303–334, 2001.

[15]G. Erlebacher, M.Y. Hussaini, C.G. Speziale, and T.A. Zang. Toward the large-eddy simulation of compressible turbulent flows. *Journal of Fluid Mechanics*, 238:155–185, 1992.

[16]C. Fureby. On subgrid scale modeling in large eddy simulations of compressible fluid flow. *Physics of Fluids A*, 8(5):1301–1311, 1996.

[17]M. Martin, U. Piomelli, and G. Candler. Subgrid-scale models for compressible large-eddy simulations. *Theoretical and Computational Fluid Dynamics*, 13(5):361–376, February 2000.

[18]N. Okong'o and J. Bellan. A priori subgrid analysis of temporal mixing layers with evaporating droplets. *Physics of Fluids*, 12(6):1573–1591, June 2000.

[19]A. Leboissetier, N. Okong'o, and J. Bellan. Consistent large eddy simulation of a temporal mixing layer laden with evaporating drops. Part 2: *A Posteriori* analysis. To be Submitted, 2004.

[20]C. Crowe, J. Chung, and T. Troutt. Particle mixing in free shear flows. *Progress in Energy and Combustion Science*, 14:171–194, 1998.

[21]T.J. Poinsot and S.K. Lele. Boundary conditions for direct simulations of compressible viscous flows. *Journal of Computational Physics*, 101:104–129, 1992.

[22]R.D. Moser and M.M. Rogers. Mixing transition and the cascade to small scales in a plane mixing layer. *Physics of Fluids A*, 3(5):1128–1134, 1991.

[23]C.A. Kennedy and M.H. Carpenter. Several new numerical methods for compressible shear layer simulations. *Applied Numerical Mathematics*, 14:397–433, 1994.

[24]J. Smagorinksy. Some historical remarks on the use of nonlinear viscosities. In B. Galperin and S.A. Orszag, editors, *Large Eddy Simulation of Complex Engineering and Geophysical Flows*, chapter 1, pages 3–36. Cambridge University Press, 1993.

[25]A. Yoshizawa. Statistical theory for compressible turbulent shear flows, with the application to subgrid modeling. *Physics of Fluids*, 29(7):2152–2164, 1986.

[26]R.A. Clark, J.H. Ferziger, and W.C. Reynolds. Evaluation of subgrid-scale models using an accurately simulated turbulent flow. *Journal of Fluid Mechanics*, 91(1):1–16, 1979.

[27]J. Bardina, J.H. Ferziger, and W.C. Reynolds. Improved subgrid scale models for large eddy simulation. Technical Report 80-1357, AIAA, 1980.

[28]M. Germano, U. Piomelli, P. Moin, and W. Cabot. A dynamic subgrid-scale eddy viscosity model. *Physics of Fluids A*, 3(7):1760–1765, 1991.

[29]B. Vreman, B. Geurts, and H. Kuerten. Large-eddy simulation of the turbulent mixing layer. *Journal of Fluid Mechanics*, 339:357–390, 1997.

[30]D.K. Lilly. A proposed modification of the Germano subgrid-scale closure method. *Physics of Fluids A*, 4(3):633–635, March 1992.

[31]J.O. Hirshfelder, C.F. Curtis, and R.B. Bird. *Molecular Theory of Gases and Liquids*. John Wiley and Sons, 1954.

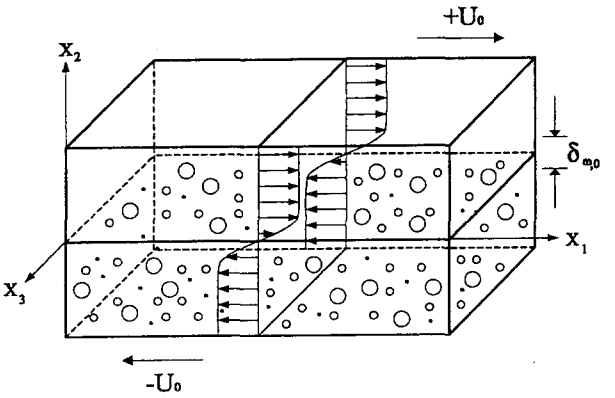

Fig. 1 Mixing Layer Configuration

Run	TP600a2	TP600a5
Re_0	600	600
ML_0	0.2	0.5
$N_{d,0}$	2993630	7484075
t^*_{trans}	105	105
$\delta_m/\delta_{\omega,0}$ at t^*_{trans}	2.627	2.613
Re_m at t^*_{trans}	1576	1568
N_d at t^*_{trans}	2876604	7448608
CPU-hours (estimated)	2252	2981

t^*_{trans}: transition time (dimensionless, rounded to nearest t^* divisible by 5), $t^* = t\Delta U_0/\delta_{\omega,0}$; $\mathrm{Re}_m = \rho_0 \Delta U_0 \delta_m/\mu$; CPU hours are estimates on 64 processors of an SGI Origin 2000

Table 1 Summary of DNS database.

TP600a2	$N_{cd,0}$=374189			
SGS Model	$\delta_m/\delta_{\omega,0}$	N_{cd}	N_{cd} within layer	CPU (h)
FC-DNS	2.631	359550	200510	–
SMD	2.223	351836	163746	20
GRD	2.102	358377	227931	20
SSC	2.270	351140	183016	19
TP600a5	$N_{cd,0}$=935498			
SGS Model	$\delta_m/\delta_{\omega,0}$	N_{cd}	N_{cd} within layer	CPU (h)
FC-DNS	2.617	931048	507595	–
SMD	2.230	929271	455615	37
GRD	2.313	931462	529789	37
SSC	2.152	929275	381218	38

$\delta_m/\delta_{\omega,0}$ and N_{cd} at transition time t^*_{trans}=105. CPU hours on SGI Origin2000.

Table 2 FC-DNS and LES corresponding to DNS cases listed in Table 1; N_R=8.

TP600a2	Average			
	FC-DNS	GRD	SMD	SSC
g_{III}	17504	8973	12551	8787
$g_{I,chpot}$	-10270	-5129	-7512	-5105
g_{II}	-308	-41	10	-111
g_{visc}	600	423	366	360
g_{mass}	74	103	74	74
$g_{I,kine}$	73	30	85	23
g_{temp}	22	18	28	19
g	7694	4377	5603	4047
TP600a2	RMS			
	FC-DNS	GRD	SMD	SSC
g_{III}	33227	20240	28312	20424
$g_{I,chpot}$	20414	12685	17856	12859
g_{II}	1881	1715	1943	1524
g_{visc}	1109	825	640	736
g_{mass}	313	524	388	377
$g_{I,kine}$	191	147	274	141
g_{temp}	46	42	76	45
g	13588	8419	11409	8316
TP600a5	Average			
	FC-DNS	GRD	SMD	SSC
g_{III}	33900	15644	22101	12464
$g_{I,chpot}$	-19485	-8269	-12327	-6131
g_{II}	-844	147	442	153
g_{visc}	663	530	348	302
g_{mass}	96	122	81	72
$g_{I,kine}$	158	45	107	13
g_{temp}	26	20	24	17
g	14514	8240	10778	6889
TP600a5	RMS			
	FC-DNS	GRD	SMD	SSC
g_{III}	58899	33308	55526	28605
$g_{I,chpot}$	36988	21454	35621	18926
g_{II}	5553	4999	7280	4278
g_{visc}	1208	990	636	607
g_{mass}	430	669	515	379
$g_{I,kine}$	393	261	464	228
g_{temp}	58	50	84	44
g	22849	13843	23024	11353

Table 3 Entropy production ($\mathrm{W/m^3K}$) of FC-DNS and LES, t^*=105.

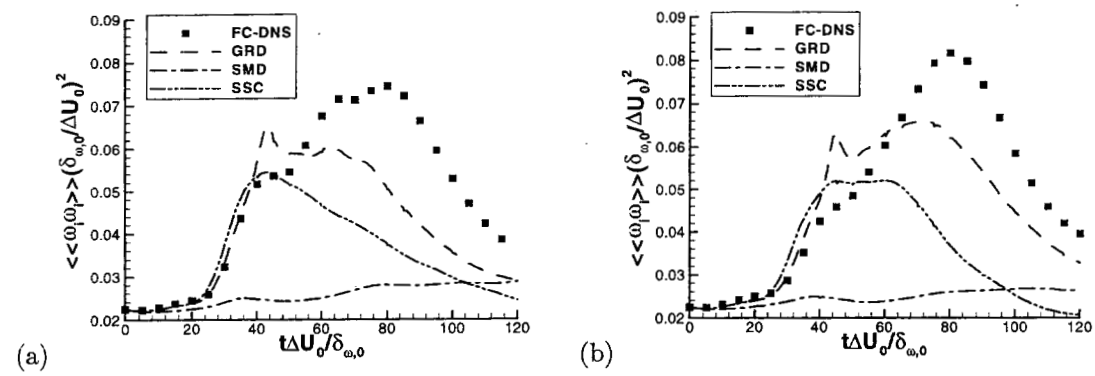

Fig. 2 Evolution of domain-averaged enstrophy for (a) TP600a2 and (b) TP600a5.

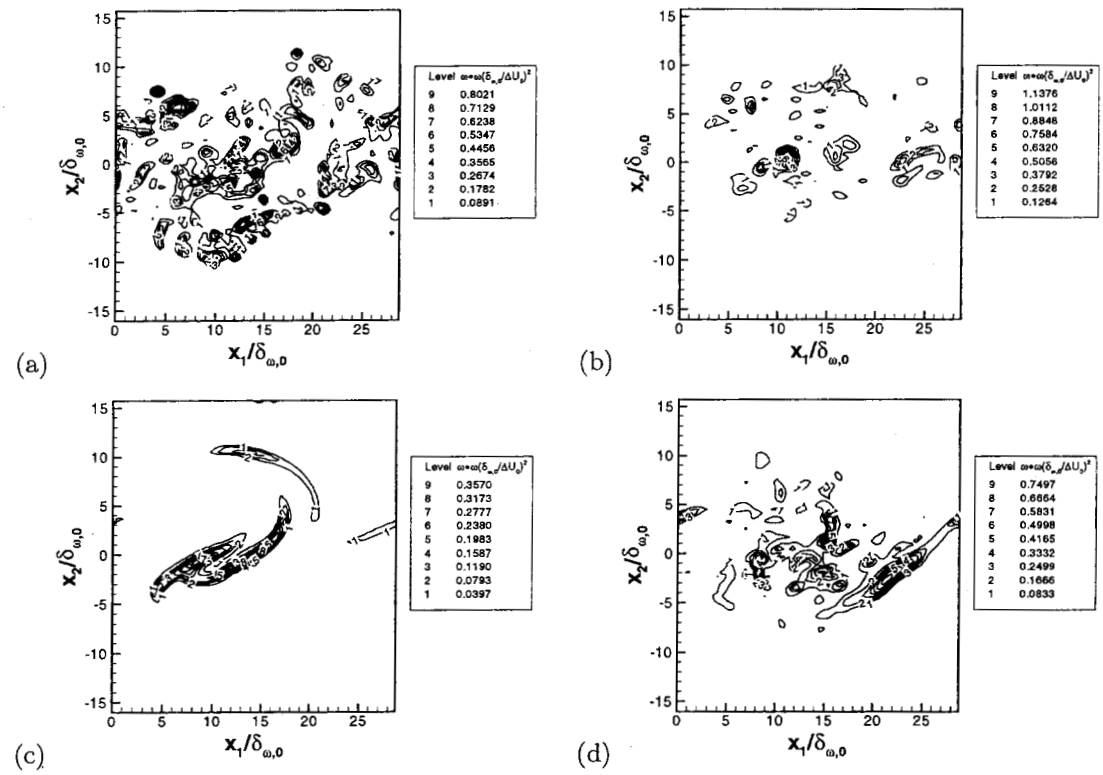

Fig. 3 Enstrophy, TP600a2 at t^*=105, Between-the-braid plane: (a) FC-DNS, (b) GRD, (c) SMD, and (d) SSC.

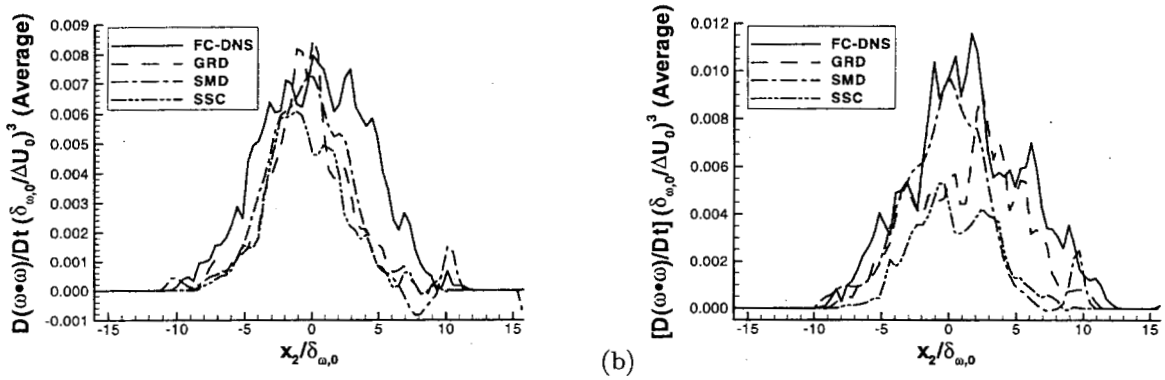

Fig. 4 Enstrophy budget at t^*=105, Averages in homogeneous planes: (a) TP600a2 and (b) TP600a5.

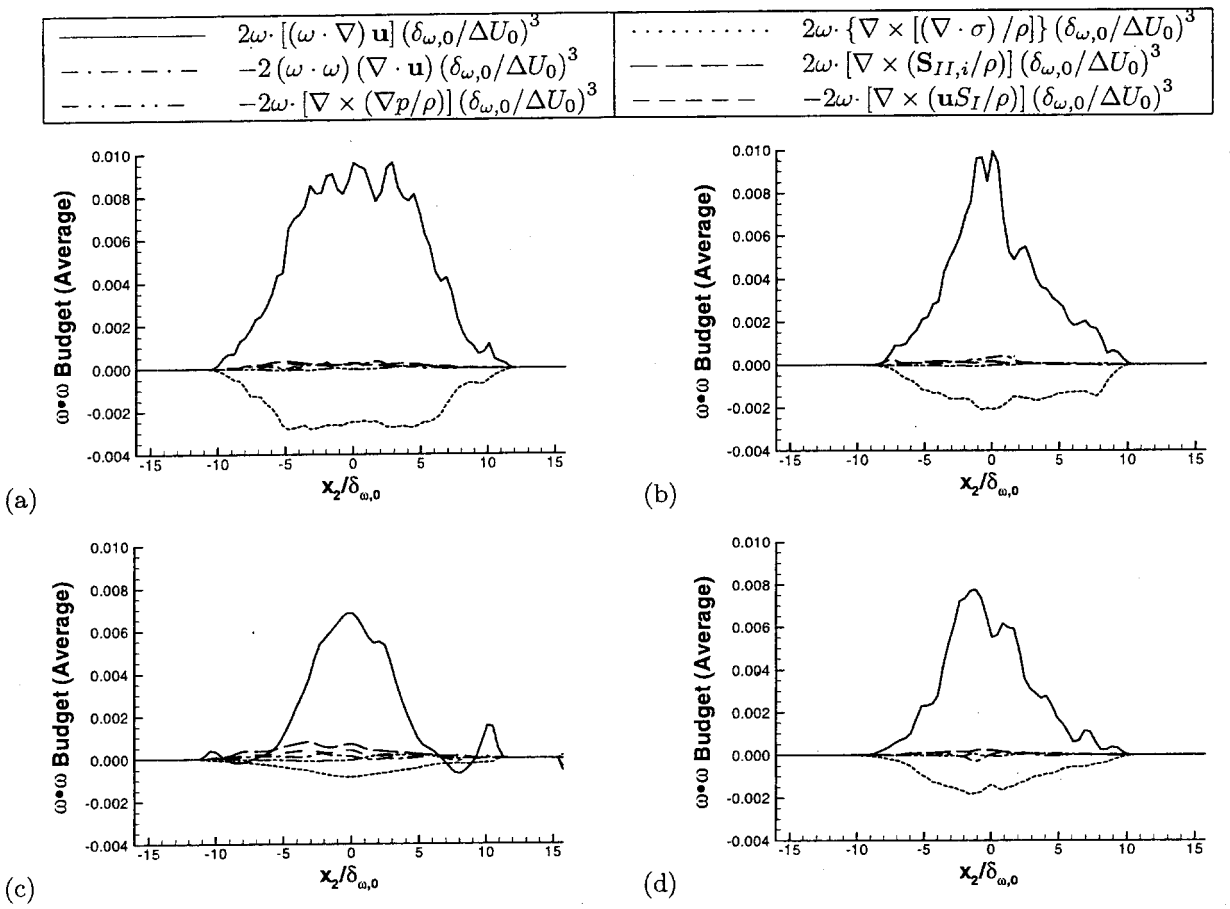

Fig. 5 Enstrophy budget, TP600a2 at t^*=105, Averages in homogeneous planes: (a) FC-DNS, (b) GRD, (c) SMD, and (d) SSC.

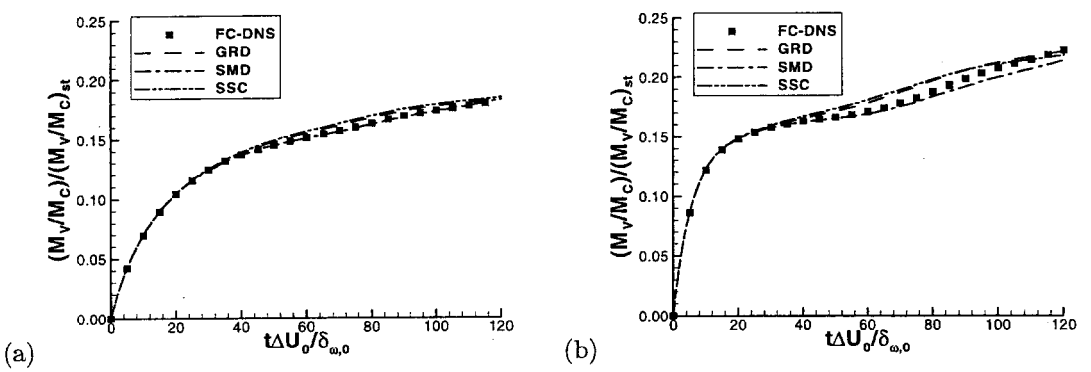

Fig. 6 Evolution of global equivalence ratio: (a) TP600a2 and (b) TP600a5.

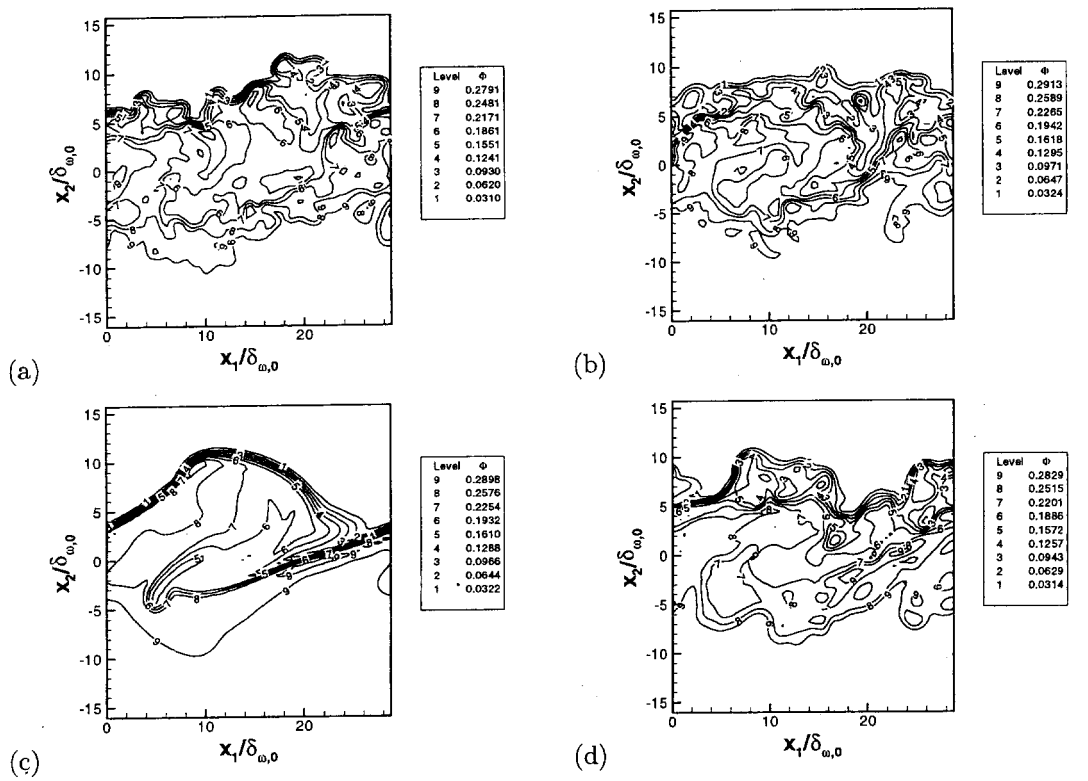

Fig. 7 Equivalence Ratio, TP600a2 at t^*=105, Between-the-braid plane: (a) FC-DNS, (b) GRD, (c) SMD, and (d) SSC.

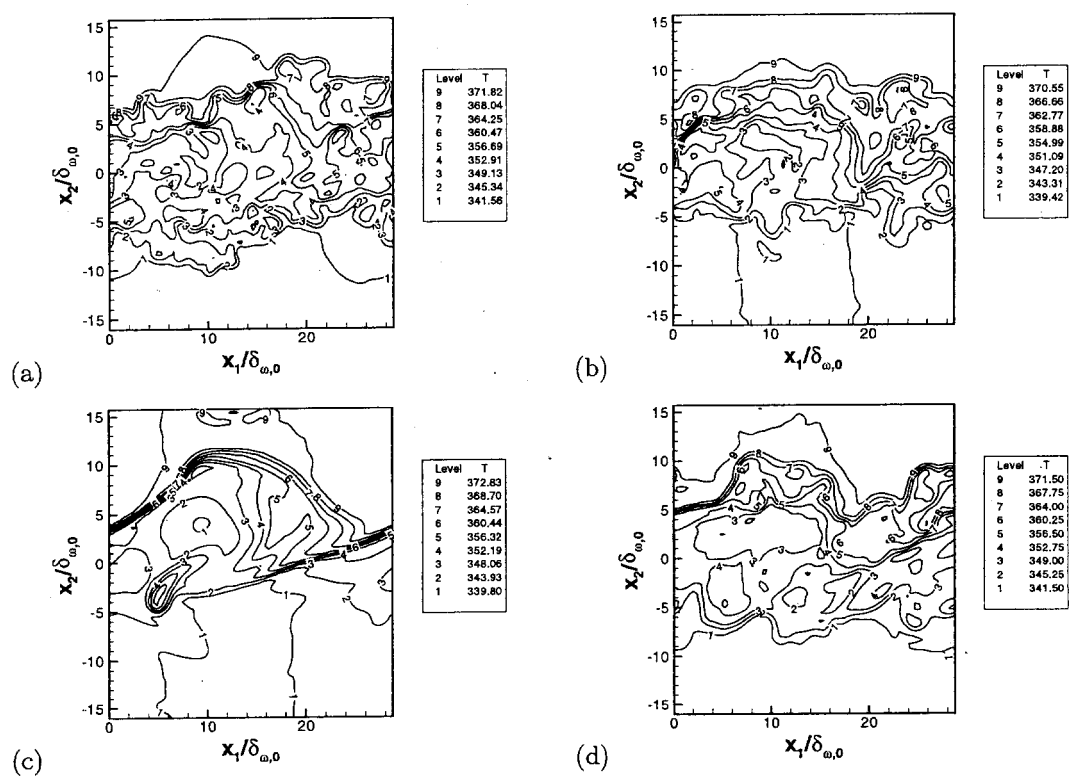

Fig. 8 Temperature (K), TP600a2 at t^*=105, Between-the-braid plane: (a) FC-DNS, (b) GRD, (c) SMD, and (d) SSC.

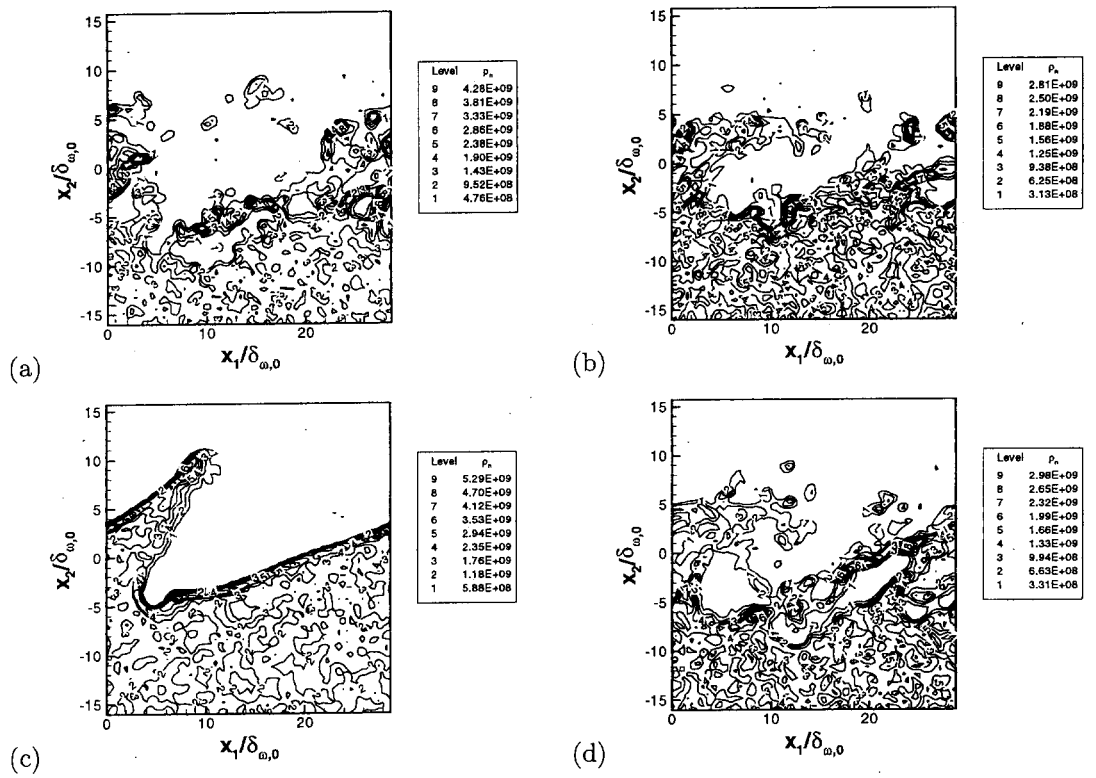

Fig. 9 Drop number density (m^{-3}), TP600a2 at t^*=105, Between-the-braid plane: (a) FC-DNS, (b) GRD, (c) SMD, and (d) SSC.

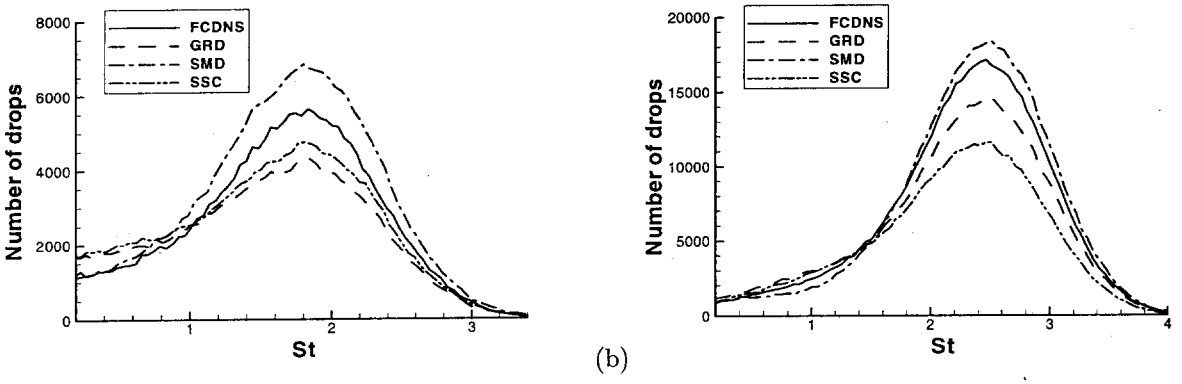

Fig. 10 Number of drops within layer versus Stokes number: (a) TP600a2 and (b) TP600a5.

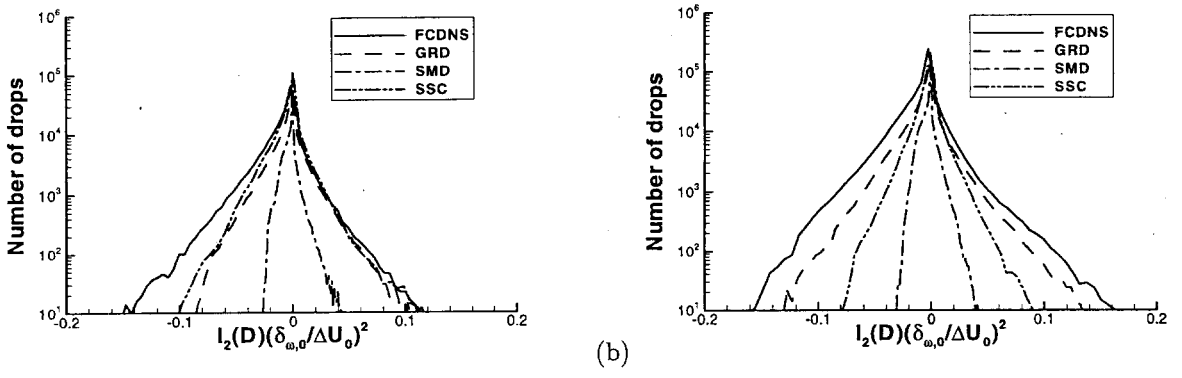

Fig. 11 Number of drops within layer versus I_2(D): (a) TP600a2 and (b) TP600a5.

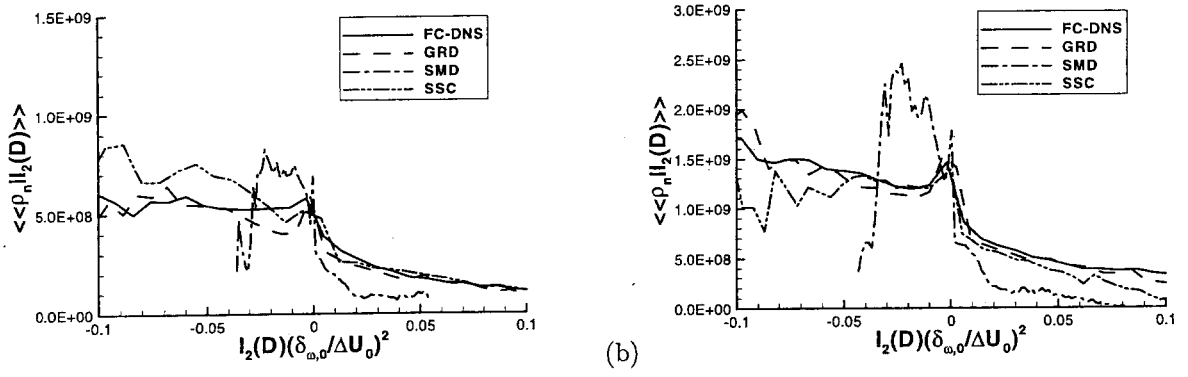

Fig. 12 Drop number density within layer (m^{-3}), conditionally averaged on I_2(D): (a) TP600a2 and (b) TP600a5.

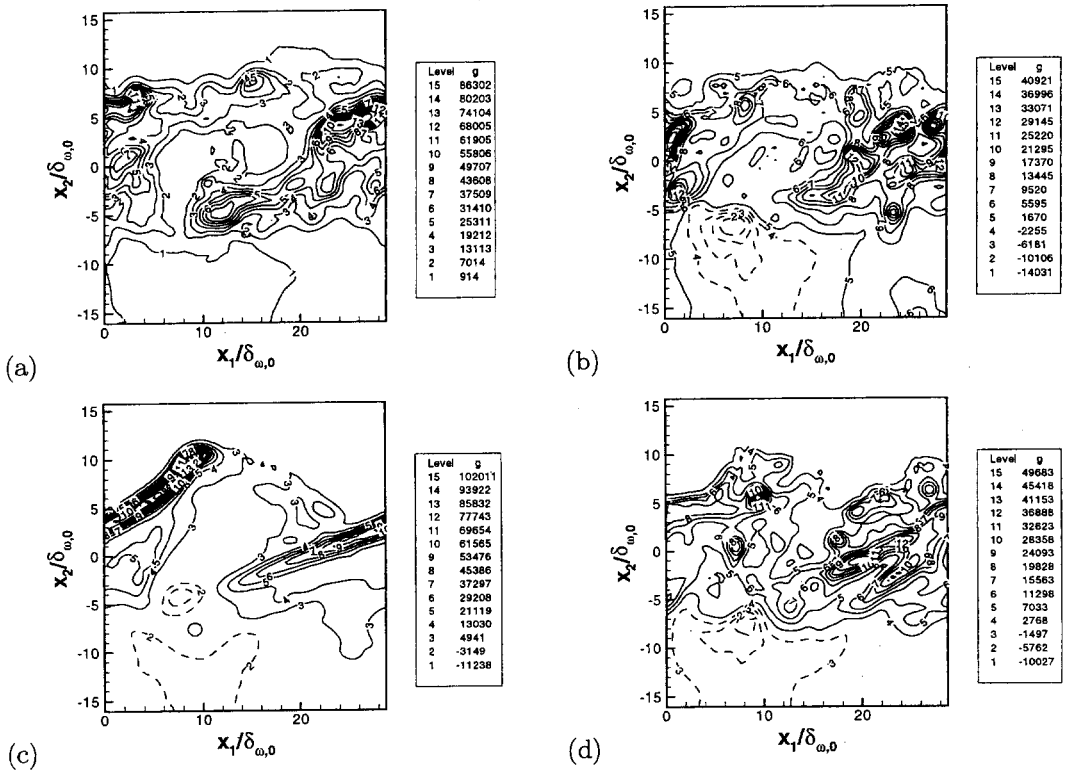

Fig. 13 Dissipation (W/m^3K), TP600a2 at t^*=105, Between-the-braid plane: (a) FC-DNS, (b) GRD, (c) SMD, and (d) SSC. Dashed lines denote negative values.